Superior Stability Secured by a Four-Phase Cathode Electrolyte Interface on a Ni-Rich Cathode for Lithium Ion Batteries

Shaodian Yang,[†,‡,⊥] Qinglu Fan,[†,‡,⊥] Zhicong Shi,*[,†,‡] Liying Liu,*[,†,‡] Jun Liu,[†,‡] Xi Ke,[†,‡] Jianping Liu,[†,‡] Chaoyu Hong,[§] Yong Yang,[§] and Zaiping Guo*[,‖]

[†]Smart Energy Research Centre, School of Materials and Energy and [‡]Guangdong Engineering Technology Research Center for New Energy Materials and Devices, Guangdong University of Technology, Guangzhou 510006, China
[§]State Key Lab for Physical Chemistry of Solid Surfaces, Department of Chemistry, College of Chemistry and Chemical Engineering, Xiamen University, Xiamen 361005, China
[‖]Institute for Superconducting & Electronic Materials, School of Mechanical, Materials and Mechatronics Engineering, University of Wollongong, Wollongong, NSW 2522, Australia

Ⓢ Supporting Information

ABSTRACT: A multifunctional coating with high ionic and electronic conductivity is constructed on the surface of $LiNi_{0.8}Co_{0.1}Mn_{0.1}O_2$ (NCM) to boost the battery stability upon cycling and during storage as well. Phosphoric acid reacts with residual lithium species on the pristine NCM to form a Li_3PO_4 coating with extra carbon nanotubes (CNTs) penetrating through, which shows high ionic and electronic conductivity. NCM, Li_3PO_4, CNTs, and the electrolyte jointly form a four-phase cathode electrolyte interface, which plays a key role in the great enhancement of capacity retention, from 50.3% for pristine NCM to 84.8% for the modified one after 500 cycles at 0.5C at room temperature. The modified NCM also delivers superior electrochemical performances at a high cut-off voltage (4.5 V), high temperature (55 °C), and high rate (10C). Furthermore, it can deliver 154.2 mA h g^{-1} at the 500th cycle after exposed to air with high humidity for 2 weeks. These results demonstrate that the well-constructed multifunctional coating can remarkably enhance the chemical and electrochemical performances of NCM. The improved cycling, storage, and rate performance are attributed to the four-phase cathode electrolyte interface delivering high electron and ionic conductivity and securing the cathode against attack. This work broadens the horizon for constructing effective electrode/electrolyte interfaces for electrochemical energy storage and conversion.

KEYWORDS: *lithium ion batteries, $LiNi_{0.8}Co_{0.1}Mn_{0.1}O_2$, stability, cathode electrolyte interface, storage performance*
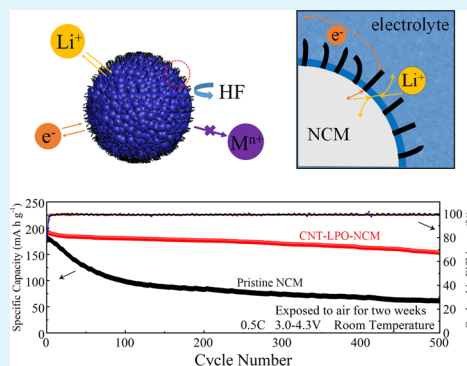
■ INTRODUCTION

With the rapid development of 3C (computer, communication, and consumer electronics) products and electric vehicles, lithium-ion rechargeable batteries (LIBs) play an indispensable role in the modern society. In addition, layered Ni-rich oxides ($LiNi_xCo_yMn_zO_2$) have been deemed as the most promising next-generation cathode materials for LIBs because of their high discharge capacity.[1−5] Among them, $LiNi_{0.5}Co_{0.2}Mn_{0.3}O_2$ and $LiNi_{0.6}Co_{0.2}Mn_{0.2}O_2$ have been commercialized with excellent stability, but the relatively low specific capacity (160 mA h g^{-1}) impedes further improvement in battery performances.[6]

Previous studies have reported that increasing the Ni content in $LiNi_xCo_yMn_zO_2$ is beneficial to the specific capacity.[7−9] The reasons are ascribed to the oxidation of nickel ions from Ni^{2+} to Ni^{3+} and then to Ni^{4+} during Li^+ de-intercalation/intercalation and the transition between Co^{3+} and Co^{4+} under a high cut-off voltage.[10,11] However, high cut-off voltages lead to the accelerated decomposition of the $LiPF_6$ electrolyte into LiF and PF_5, and PF_5 preferably reacts with

H_2O to produce HF, which dissolves the metal oxide into electrolyte.[4,12,13] Besides, the ionic radius of Ni^{2+} (0.69 Å) is similar to that of Li^+ (0.76 Å); therefore, the cation mixing increases with an increased Ni^{2+} content.[14−16] Thermal instability and structural instability caused by increased HF corrosion and cation mixing may result in an uncontrolled heat release inside the battery and even the risk of explosion.[17,18] Although $LiNi_{0.8}Co_{0.1}Mn_{0.1}O_2$ (NCM) has inspired enormous research motivation, how to solve the above-mentioned problems is still a huge challenge at present.[19]

Surface-coating, as one of the breakthrough technologies, is widely used to circumvent the drawbacks of layered Ni-rich oxides.[20−25] Various coating materials including metal oxides, metal fluorides, and metal phosphate have been extensively studied. The surface-coating layers effectively hinder side reactions between the active material and the electrolyte, so as

Scheme 1. Schematic Diagram of the Synthesis Process of Pristine NCM, LPO-NCM, and CNT-LPO-NCM
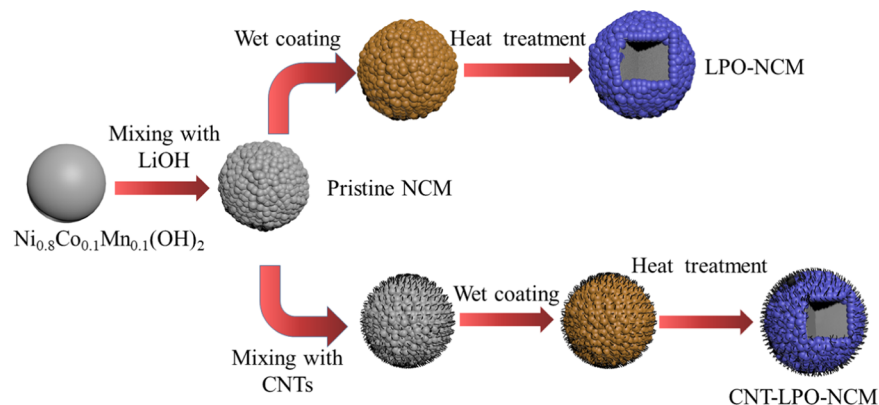
to improve the thermal stability of $LiNi_{0.6}Co_{0.2}Mn_{0.2}O_2$, and the possible reasons have been reported in former literature.[18,26] Furthermore, the high ionic conductivity of the Li_3PO_4 coating has also been pointed out.[27] However, phosphate is really a poor electronic conductor, which forms an energy barrier on the surface of NCM. Adding highly conductive materials is one of the effective ways to improve its electronic conductivity. Until now, several composite coatings containing a metal phosphate and other good electronic conductors have been studied and the multifunctional coatings are reported with advantages of reduced residual lithium on the surface, blocked direct contact of the active material with the electrolyte, and enhanced electronic as well as ion conductions.[22,28]

In this study, we construct a Li_3PO_4 and carbon nanotube (CNT) multifunctional coating on the surface of pristine NCM by the wet chemical method. CNTs were uniformly distributed and fixed in the Li_3PO_4 nanocoating on the surface of NCM. Effects of the multifunctional coating on the physical and electrochemical performances of NCM were investigated. It was confirmed that the modified CNT-LPO-NCM sample with high electronic and ionic conductivities possesses improved thermal stability and storage performance and exhibits excellent cycle stability and rate performance at both low (4.3 V) and high (4.5 V) cut-off voltages, even at high temperature (55 °C). A four-phase cathode electrolyte interface model was proposed to better understand the working mechanism of the multifunctional coating on the NCM cathode materials.

■ EXPERIMENTAL SECTION

Synthesis of Powder Materials. Pristine NCM was synthesized as described in a published paper.[14] The Li_3PO_4-coated NCM (LPO-NCM) was prepared by the following process.[15] H_3PO_4 (0.047 g) was dissolved in 40 mL of ethanol. Then, 4 g of the pristine NCM sample was added to the above solution, heating and stirring them at 80 °C until ethanol was completely evaporated. Finally, heat treatment at 500 °C for 300 min in Ar atmosphere was carried out to achieve the final LPO-NCM sample.

The synthesis of CNT-LPO-NCM was similar to that of LPO-NCM. The only difference was the addition of a ground mixture of 0.04 g CNT and 4 g pristine NCM instead of pristine NCM into the phosphate alcohol solution.

A schematic diagram of the synthesis process for all powder materials is illustrated in Scheme 1.

Material Characterization. The crystalline structures were identified by X-ray diffraction (XRD, Bruker, D8 ADVANCE) with Cu Kα radiation. The XRD data for Rietveld refinement were recorded in the range of 10−90° with a step length of 0.02° min⁻¹. High-resolution neutron powder diffraction data were collected at the VULCAN instrument at the Spallation Neutron Sources (SNS), Oak Ridge National Laboratory (ORNL).[14,29] Data were processed by the VDRIVE software;[30] quantitative structural analysis was carried out using the General Structure Analysis System (GSAS).[31,32] Field-emission scanning electron microscopy (FE-SEM, JEOL, JSM-6700F) and field-emission transmission electron microscopy (TEM, JEOL, 2010F) with energy-dispersive spectroscopy (EDS) mapping were used to investigate morphological features of pristine NCM, LPO-NCM, and CNT-LPO-NCM powders. The surface area was measured with a specific surface analyzer (SSA, BeiShiDe, 3H-2000). The X-ray photoelectron spectroscopy (XPS, Thermos Fisher, ESCAlab250) measurement was carried out to analyze the chemical information on material surfaces. The differential scanning calorimetry (NETZSCH, STA409PC) test conditions were 30−400 °C at a heating rate of 5 °C min⁻¹. The dissolved cation concentration in the electrolyte was tested by inductively coupled plasma mass spectrometry (ICP-MS, Thermos Fisher, ICAP RQ).

Electrochemical Measurements. Preparation of the cathode and assembly of the half cell (Li metal foil as the anode) and full cell (graphite as the anode) were described previously.[14] Pristine NCM and CNT-LPO-NCM were stored in open-capped glass vials for 2 weeks at room temperature with a humidity of 65% before storage performance testing. The half or full coin cells were tested on a BTS-5 V10 mA cell testing instrument (Land Electronic Co., Ltd.) at different rates of 0.5C, 1C, 2C, 5C, and 10C (1C = 200 mA h g⁻¹) in the voltage ranges of 3.0−4.3 and 3.0−4.5 V versus Li/Li⁺ at room temperature or at high temperature (55 °C). Before cycling, they were charged−discharged at 0.2C for the initial two cycles. Cyclic voltammetry (CV) data were collected between 3.0 and 4.5 V at a rate of 0.1 mV s⁻¹. The electrochemical impedance spectra (EIS) were conducted in a frequency range from 5 MHz to 1 mHz. Both CV and EIS were performed on an electrochemical instrument (Solartron, 1287&1260).

■ RESULTS AND DISCUSSION

As shown in Figure 1a, all samples have typical layered structures like a hexagonal α-NaFeO₂ single phase with the $R\bar{3}m$ space group.[33,34] The (108)/(110) distinct peak splitting also demonstrate that all materials possess well-crystallized layered structures, and no extra peaks can be detected. Figure 1b−d provide Rietveld refinements for three samples. Compared with pristine NCM, LPO-NCM and CNT-LPO-NCM keep almost unchanged $I(003)/(104)$ values, which reflect the degree of Li/Ni cation mixing. All c/a ratios are higher than 4.899, indicating that all samples have well-crystallized layered structures.[35,36] Based on the above discussion, it can be concluded that neither the Li_3PO_4 nor
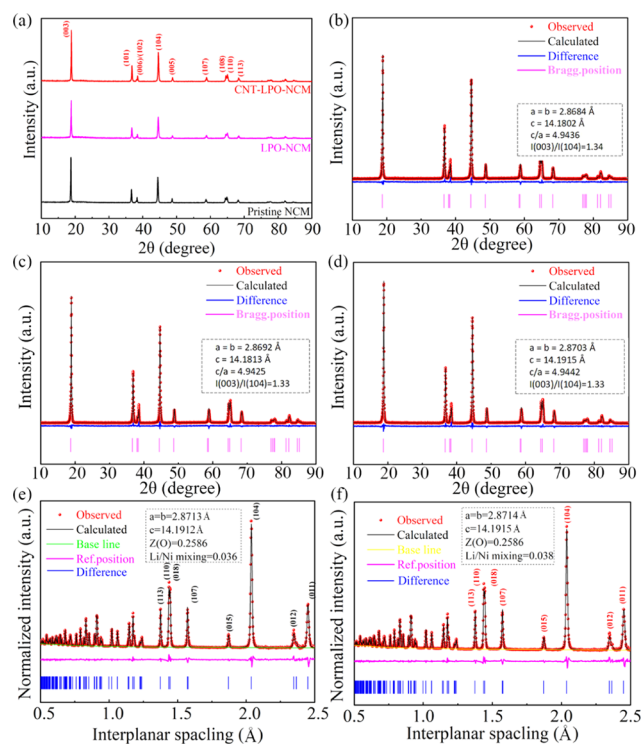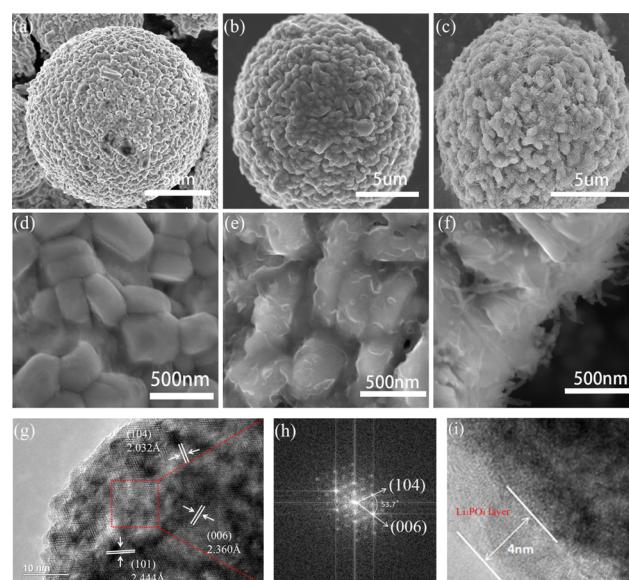
Figure 1. XRD patterns (a) and Rietveld refinements for pristine NCM (b), LPO-NCM (c), and CNT-LPO-NCM (d) with the reference NCM diffraction pattern. The Rietveld refinements of neutron diffraction data for pristine NCM (e) and CNT-LPO-NCM (f).

Figure 2. SEM images of pristine NCM (a, d), LPO-NCM (b, e), and CNT-LPO-NCM (c, f). Pristine NCM (g) and the corresponding FFT patterns (h) taken from the selected region in (g). TEM images of CNT-LPO-NCM (i).

the CNT-LPO coating layer affects the lattice structure of NCM.

To further explore the Li/Ni cation mixing, a neutron diffraction test was carried out on pristine NCM and CNT-LPO-NCM.[5,37] The refinements of neutron diffraction data are given in Figure 1e,f. As Figure 1e,f show, there are no significant changes in the a, b, and c values, which is consistent with the XRD results. It is worth noting that a slight increase in Li/Ni mixing for CNT-LPO-NCM is confirmed, which may result from the heat-treatment process to form the multifunctional coating.

The spherical secondary particles in Figure 2a−c are all about 10 μm and the particle sizes are not affected by coatings. Partial lithium residue and a coating on the pristine NCM and LPO-NCM surface can be clearly seen in Figure 2d,e, respectively. Figure S1a shows the EDS mapping results in which the P element is uniformly distributed in LPO-NCM, inferring a uniformly coated Li_3PO_4 layer. In Figure 2f, a coating similar to that in Figure 2e combined with CNTs with 500 nm length is distributed on the surfaces of CNT-LPO-NCM. The synergy between the ultrahigh electron conduction of CNTs and the ion conduction of Li_3PO_4 may be advantageous for NCM. Figure S1b shows the EDS mapping of CNT-LPO-NCM, in which not only Ni, Co, Mn, and O but also P and C elements are uniformly distributed. This further confirms that the added CNTs are uniformly distributed on the CNT-LPO-NCM surfaces together with the Li_3PO_4 coating. More details of the layered oxides and coatings can be observed by TEM results. The well-arranged lattice fringes in Figure 2g indicate the high degree of crystallinity of NCM, and the fast Fourier transform (FFT) results in Figure 2h also

confirm the layered structure. The measured interplanar spacing widths of 2.032, 2.360, and 2.444 Å are separately corresponding to the crystal faces (104), (006), and (101). From Figure 2i, we can see that CNT-LPO-NCM has a uniform coating with a thickness of 4 nm.

It can be seen from Table 1 that LPO-NCM has the smallest specific surface area. Although Li_3PO_4 inhibits the corrosion of

Table 1. Specific Surface Areas of Pristine NCM, LPO-NCM, and CNT-LPO-NCM

sample	specific surface area (m^2 g^{-1})
pristine NCM	0.58
LPO-NCM	0.27
CNT-LPO-NCM	1.56

active substances by HF, the conductivity of Li_3PO_4 is poor, which is not conducive to the transmission of electrons at the interface. The specific surface of CNT-LPO-NCM is the largest because of the contribution of CNTs, and so side reactions will not increase with increased specific surface areas in this cast. CNTs provide a large number of electron transport channels.

The C 1s spectra of both samples are obviously different in Figure 3a. The binding energy of C 1s at 289.8 eV can be attributed to the residual lithium (Li_2CO_3) on the surface of pristine NCM, whereas no corresponding peaks are found in CNT-LPO-NCM, which further demonstrates that H_3PO_4 does reduce the residual lithium on the particle surface. After adding CNTs, not only the C−C peak (284.8 eV) but also the C=O peak (288.0 eV) appeared. The C−C peak is assigned to the CNT on the CNT-LPO-NCM surface, and C=O is produced by the oxidation of the terminal C during the heat treatment. Besides the peaks at 531.4 eV and 528.6 eV in the O 1s spectrum corresponding to the residual lithium (Li_2CO_3, LiOH) and lattice oxygen of NCM, a new peak at 533.0 eV for CNT-LPO-NCM occurs in Figure 3b, which corresponds to that of Li_3PO_4.[26] The binding energy of P 2p at 133.1 eV in
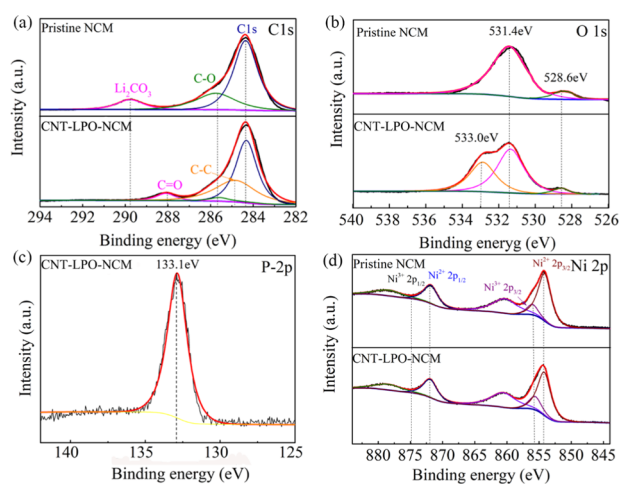
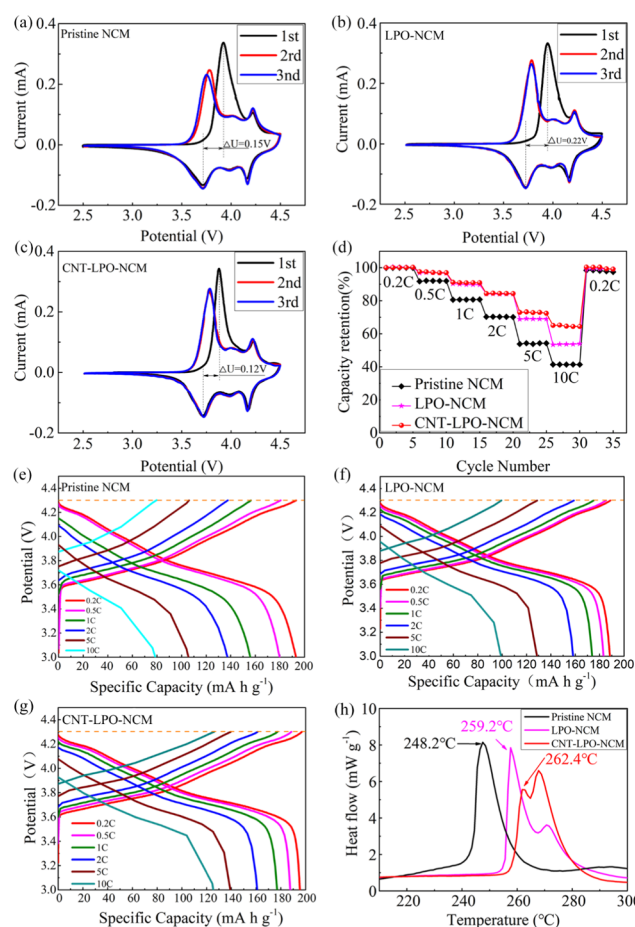**Figure 3.** XPS spectra of pristine NCM and CNT-LPO-NCM: (a) C 1s, (b) O 1s, (c) P 2p, and (d) Ni 2p.

Figure 4. First three cycles' voltammetry curves for pristine NCM (a), LPO-NCM (b), and CNT-LPO-NCM (c). Capacity retention of all samples at various current densities (d). Charge−discharge curves at different rates between 3.0 and 4.3 V at room temperature for pristine NCM (e), LPO-NCM (f), and CNT-LPO-NCM (g). Differential scanning calorimetry traces showing the heat flow from the reaction of the electrolyte with pristine NCM, LPO-NCM, and CNT-LPO-NCM charged to 4.3 V (h).

Figure 3c belongs to PO_4^{3-}. In combination with Figure 3b,c, it can be confirmed that Li_3PO_4 is formed and coated on the CNT-LPO-NCM surfaces. Ni 2p (Figure 3d), Co 2p, and Mn 2p (Figure S4) spectra of pristine NCM and CNT-LPO-NCM did not change significantly, indicating that H_3PO_4 did not change the chemical environments on the surface of NCM. The XPS results are in line with experimental expectations.

Figure 4a−c provide CV curves of pristine NCM, LPO-NCM, and CNT-LPO-NCM between 3.0 and 4.5 V (versus Li/Li^+). All samples have significant redox peaks due to the oxidation/reduction of Ni^{2+}/Ni^{4+} and Co^{3+}/Co^{4+} corresponding to the Li^+ extracting/embedding process.[20] The three pairs of oxidation and reduction peaks on their second and third cycles are caused by three phase transitions during the charge−discharge process. As Figure 4a−c show, the overlaps of CV curves for LPO-NCM and CNT-LPO-NCM better indicate the improved electrochemical reversibility. It is worth noting that there are large differences in the oxidation−reduction potential ΔV in the first cycles. The ΔV of LPO-NCM is the largest among them because of the poor electronic conductivity of the Li_3PO_4 coating,[38] whereas CNT-LPO-NCM possesses the smallest ΔV owing to CNTs providing a great deal of electron channels.

Figure 4d−g demonstrate the rate properties and corresponding charge−discharge profiles in the voltage range of 3.0−4.3 V. Compared to pristine NCM, both modified samples deliver better rate performances, especially at 5C and 10C for CNT-LPO-NCM (Figure 4d). The capacity retention of CNT-LPO-NCM is 63.9% at 10C with a discharge capacity of 123.7 mA h g^{-1} as a result of the synergistic effect of CNTs and Li_3PO_4, much higher than the values of 52.4 and 42.2% for LPO-NCM and pristine NCM, respectively. Figure 4e−g also illustrate that CNT-LPO-NCM has a significantly higher discharge specific capacity whether at low or high rates.

Figure 5a,b present the cycling stability of all samples tested under different cut-off voltages of 4.3 and 4.5 V at room temperature. The cycle stability of CNT-LPO-NCM is greatly enhanced both at low (4.3 V) and high (4.5 V) cut-off voltages. At a low cut-off voltage of 4.3 V, the discharge capacity of pristine NCM declines from 181.4 to 90.4 mA h g^{-1} after 500 cycles with a capacity retention of 50.3%. However, the initial discharge capacity of LPO-NCM with the Li_3PO_4 coating is 189.2 mA h g^{-1} with a capacity retention of 76.4%

after 500 cycles. CNT-LPO-NCM exhibits the most excellent cycling stability with an initial discharge capacity of 202.6 mA h g^{-1} and a capacity retention of 84.8% after 500 cycles, and the discharge specific capacities do not substantially decrease in the first 200 cycles. The corresponding initial charge−discharge curves in Figure S2 show that the initial coulomb efficiencies and discharge specific capacities of pristine NCM, LPO-NCM, and CNT-LPO-NCM are 74.8, 80.7, 85.1% and 184.8, 193.8, and 202.8 mA h g^{-1}, respectively. At a high cut-off voltage of 4.5 V, the improvements in cycling stability improvements for CNT-LPO-NCM become more prominent. As shown in Figure 5b, the discharge capacities of pristine NCM, LPO-NCM, and CNT-LPO-NCM are separately 72.3, 120.4, and 142.8 mA h g^{-1} after 500 cycles, corresponding to capacity retention rates of 35.1, 57.1, and 68.6%, respectively.

Coin cells of the three samples were also tested in an incubator at 55 °C to investigate the high-temperature cycle stability, and the results are given in Figure 5c. For pristine NCM, LPO-NCM, and CNT-LPO-NCM, the initial coulomb efficiencies and initial discharge specific capacities are separately 82.8, 86.7, and 87.2% and 193.5, 206.2, and 208.2
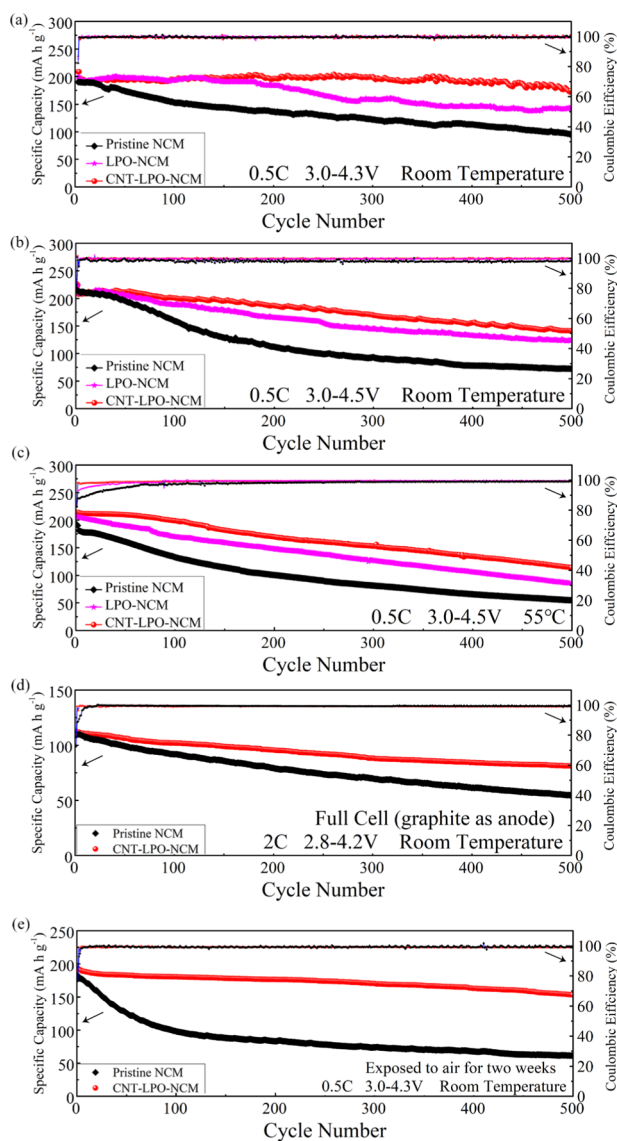
Figure 5. Cycling performances of pristine NCM, LPO-NCM, and CNT-LPO-NCM at 0.5C separately in the voltage ranges of 3.0−4.3 V (a) and 3.0−4.5 V (b) at room temperature, 3.0−4.5 V at 55 °C (c), at 2C in the voltage range of 2.8−4.2 V in a full cell (graphite as the anode) (d), and at 0.5C in the voltage range of 3.0−4.3 V at room temperature using the as-prepared cathode materials being exposed to humid air (RH 65%) for 2 weeks (e).

To further verify the possibility of CNT-LPO-NCM as the cathode material in practical batteries, full cells are assembled and tested with commercialized graphite as the anode at an N/P ratio of 1.15:1 (see Figure 5d). It is obvious that CNT-LPO-NCM delivers a significantly enhanced performance over pristine NCM in both discharge capacity and capacity retention.

Experiments on the continuous exposure of as-synthesized materials to air for 15 days have also been performed to prove the multifunctional coating's effect on the storability, and the results are given in Figure 5e. After exposure to air, the specific capacity and cyclical stability of pristine NCM decline rapidly compared to the results in Figure 5a, which proves that the layered oxide is unstable in air. The discharge specific capacity of the pristine NCM after placement is 62.1 mA h g^{-1}, corresponding to the capacity retention rate of 30.4%. However, the first discharge specific capacity of 197.2 mA h g^{-1} of CNT-LPO-NCM is not significantly different from that before placement, and the capacity retention rate is 79.7% after 500 cycles. It can be explained by the fact that the dense multifunctional coating separates the active material from harmful substances such as H_2O and CO_2 in air.

To further analyze the action mechanism of the multifunctional coating on NCM, the recycled pristine NCM and CNT-LPO-NCM were tested by SEM, XRD, and ICP. The SEM images of pristine NCM and CNT-LPO-NCM after 150 cycles at 0.5C between 3.0 and 4.3 V are illustrated in Figure 6a,b. As
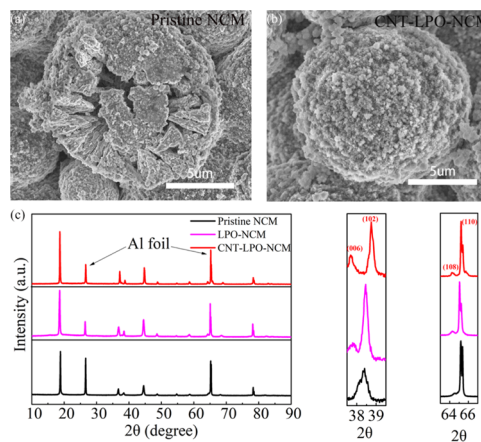
Figure 6. SEM images of pristine NCM (a) and CNT-LPO-NCM (b) after 150 cycles. XRD patterns (c) of pristine NCM, LPO-NCM, and CNT-LPO-NCM after 100 cycles.

mA h g^{-1}, respectively. The corresponding capacity retention rates after 500 cycles are 28.3, 41.2, and 60.8%, respectively.

The thermal stability of lithium batteries is a most important part of the battery performance. To discuss the effect of coating on the thermal stability of NCM, all powder samples were subjected to differential scanning calorimetry (Figure 4h). The main exothermic peak for pristine NCM is 248.2 °C, while they are separately 259.2 and 262.4 °C for LPO-NCM and CNT-LPO-NCM. In addition, the starting point of the exothermic peak for CNT-LPO-NCM is 256.8 °C, which is much higher than the value of 242.0 °C for pristine NCM. The enhanced thermal stability is attributed to the fact that the CNT-LPO coating hinders the direct reaction of the electrolyte with the active material and suppresses the precipitation of oxygen in the bulk phase.

Figure 6a,b show, there are obvious differences in their morphologies. Many cracks on the pristine NCM particle can be cleanly seen, but CNT-LPO-NCM maintains the original spherical morphology well. The multifunctional coating has a positive effect on preventing cracking and avoiding further corrosion. The XRD images of pristine NCM and CNT-LPO-NCM after 100 cycles at 0.5C between 3.0 and 4.3 V are provided in Figure 6c. In Figure 6c, the (006)/(102) and (108)/(110) split peaks of pristine NCM are almost amalgamated, whereas their splitting is obvious for CNT-LPO-NCM. The larger the distance, the more pronounced the layered structure. The results illustrate further that the CNT-LPO coating helps protect the layered structure of NCM. The effect of the CNT-LPO coating on the dissolution of metal ions was investigated by ICP-MS after 50 cycles. The cycled

batteries were disassembled, and all components were immersed in DMC for 3 days.[39] From Figure 7, we can find
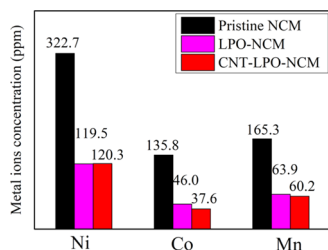

Figure 7. Dissolved transition metal cation in the electrolyte.

that the dissolved metal cations of LPO-NCM and CNT-LPO-NCM are basically the same and much less than those of pristine NCM, which confirms that the coatings can inhibit the decomposition caused by HF and reduce the dissolution of metal cations in the electrolyte, thereby improving the cycle stability. This is in line with previous experimental works.[40]

Figure 8 presents the EIS results at the charged state (4.3 V) after 5 and 50 cycles at 0.5C between 3.0 and 4.3 V. As shown
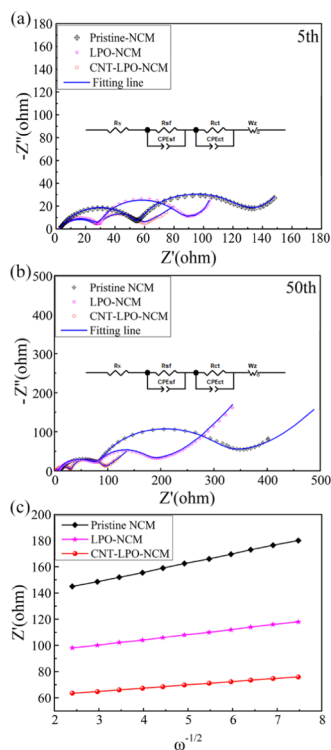

Figure 8. Nyquist plots and the fitting results of pristine NCM, LPO-NCM, and CNT-LPO-NCM after 5 cycles (a) and 50 cycles (b) at the charged state. Relationship between Z real and $\omega^{-1/2}$ of pristine NCM, LPO-NCM, and CNT-LPO-NCM (c).

in Figure 8a,b, all Nyquist diagrams consist of two semicircles and an oblique line. The first semicircles in the high-frequency region represent the Li+ migration resistance (R_{sf}) through the surface membrane on the layered Ni-rich oxides, the starting point of which represents the electrolyte resistance (R_s). The second semicircles located in the high-to-medium-frequency region are associated with the charge-transfer resistance (R_{ct}). The slant lines in the low-frequency region are related to the Warburg impedance representing the Li+ diffusion in the cathode material. The fitting results of R_s, R_{sf}, and R_{ct} are listed in Table 2. As can be seen from Table 2, the total resistances ($R_s + R_{sf} + R_{ct}$) for CNT-LPO-NCM are the smallest whether for the 5th or the 50th cycle, and the corresponding increment from the 5th to the 50th cycle is also much lower than those of others.

The lithium ion diffusion coefficient (D_{Li^+}) in the bulk phase is an important indicator of the dynamic performance of lithium-ion batteries, which can be calculated from the Warburg impedance coefficient using formulas 1 and 2 by the EIS technique[41,42]

$$D_{Li^+} = \frac{R^2 T^2}{2n^4 F^4 A^2 C_{Li^+}^2 \sigma^2} \tag{1}$$

$$Z' = R_s + R_{ct} + \sigma\omega^{-1/2} \tag{2}$$

here, R represents the gas constant, T represents the absolute temperature, F represents the Faraday constant, n represents the number of charge transfers, A is the active electrode area, and C is the concentration of lithium ions. The Warburg factor (σ) can be calculated from the fitting results in Figure 8c by formula 2.

The calculated D_{Li^+} values of pristine NCM, LPO-NCM, and CNT-LPO-NCM are 1.26×10^{-12}, 2.42×10^{-12}, and 5.91×10^{-12} cm s^{-1}, respectively. It is obvious that D_{Li^+} of CNT-LPO-NCM is the largest one. The results further confirm that the CNT and Li3PO4 composite conductive coating reduces the resistances of electrodes and increases the Li+ diffusion rate.

Based on the above discussion, CNT-LPO-NCM possesses a superior cyclical stability, rate performance, and storability, even under worse operating conditions such as a high cut-off voltage and high temperature, which may be ascribed to the following aspects. First, the inactive lithium residues (Li2CO3/LiOH) on the surface of NCM are reduced by chemical reactions. Second, the uniform and thin multifunctional coating layer protects the active material from corrosion by HF. Third, the Li3PO4 coating layer with high ionic conductivity is beneficial to Li+ delivery at the interface. Fourth, CNTs with excellent linear conductivity help improve the electron conductivity of the Li3PO4 coating and reduce the charge-transfer resistance. Finally, the combination of CNTs and Li3PO4 has some synergistic effects. CNTs are fixed by Li3PO4 on the surface of the layered oxide and do not fall off easily; the superior flexibility of CNTs may be able to reduce stress cracking of the Li3PO4 coating and maintain the integrity

Table 2. Electrochemical Impedance Spectra Fitting Results of R_s, R_{sf}, and R_{ct} of Pristine NCM, LPO-NCM, and CNT-LPO-NCM Cathode Materials after the 5th and the 50th Cycles, Respectively

	pristine NCM			LPO-NCM			CNT-LPO-NCM		
	R_s/Ω	R_{sf}/Ω	R_{ct}/Ω	R_s/Ω	R_{sf}/Ω	R_{ct}/Ω	R_s/Ω	R_{sf}/Ω	R_{ct}/Ω
5th	3.4	51.7	87.5	3.0	24.8	62.4	2.8	24.7	32.6
50th	9.4	72.1	280.5	6.1	70.2	110.1	3.4	26.8	70.2

of the multifunctional coating under a long circulation and high rate.[18,43−45] The result confirms that the CNTs composited with lithium phosphate are promising coatings for high-energy-density lithium ion batteries.

To further understand the role of the multifunctional coating, a four-phase interface model was proposed. The interface involves four phases including NCM, CNTs, Li_3PO_4, and the electrolyte. The multifunctional coating, consisting of CNTs and Li_3PO_4, helps prevent the layered oxide cathode materials from HF attack, so as to reduce the dissolution of the active material in the electrolyte (Figure 9a), which has been
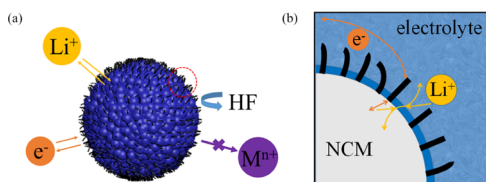
Figure 9. Schematic diagram of the working mechanism of CNT-LPO-NCM (a) and the corresponding reaction mechanism of the four-phase interface (b) obtained from the selected region in (a).

confirmed by ICP-MS tests as shown in Figure 7. CNTs connect NCM and conductive carbon black or current collectors, securing fast electron transportation (Figure 9b). Li_3PO_4 provides a large number of lithium ion channels, securing fast lithium ion migration. The four-phase cathode electrolyte interface shows a well-reduced impedance with fast transportation of ions and electrons at the same time. As a result, the NCM with the CNT-LPO coating demonstrates an excellent storage capacity, rate performance, and cycling stability at room and high temperatures.

CONCLUSIONS

A multifunctional coating, consisting of Li_3PO_4 and CNTs with high electronic and ionic conductivity, is constructed on the surface of $LiNi_{0.8}Co_{0.1}Mn_{0.1}O_2$ (NCM) as the cathode material for lithium ion batteries. CNT-LPO-NCM shows an excellent rate performance and cycle stability, even at high temperatures and high cut-off voltages, which is attributed to a four-phase cathode electrolyte interface consisting of NCM, Li_3PO_4, CNTs, and the electrolyte. A specific discharge capacity of 168.8 mA h g^{-1} after 500 cycles at 0.5C rate between 3.0 and 4.5 V is achieved for CNT-LPO-NCM. It also delivers 154.2 mA h g^{-1} at the 500th cycle after being exposed to air with high humidity for 2 weeks. The excellent electrochemical and storage performances are attributed to the multifunctional coating, the construction of a four-phase cathode electrolyte interface, and the availability of rich electronic pathways and ion channels in addition to preventing NCM from the HF attack. Constructing a multifunctional four-phase cathode electrolyte interface is an effective method to improve the electrochemical performance of Ni-rich layered oxide cathode materials for lithium ion batteries. This novel strategy may shed light on exploring high-performance electrode materials with an effective coating for electrochemical energy storage and conversion.

ASSOCIATED CONTENT

Supporting Information

The Supporting Information is available free of charge on the ACS Publications website at DOI: 10.1021/acsami.9b12578.

Mapping of LPO-NCM and CNT-LPO-NCM, initial charge−discharge curves of all samples, Rietveld refinement results of XRD data for all samples, and the TGA curves of CNTs in an air atmosphere (PDF)

AUTHOR INFORMATION

Corresponding Authors
*E-mail: zhicong@gdut.edu.cn (Z.S.).
*E-mail: liyingliusy@163.com (L.L.).
*E-mail: zguo@uow.edu.au (Z.G.).

ORCID
Zhicong Shi: 0000-0003-2360-7668
Yong Yang: 0000-0003-1145-8992
Zaiping Guo: 0000-0003-3464-5301

Author Contributions
[⊥]S.Y. and Q.F. contributed equally.

Notes
The authors declare no competing financial interest.

ACKNOWLEDGMENTS

REFERENCES

(1) de Biasi, L.; Schwarz, B.; Brezesinski, T.; Hartmann, P.; Janek, J.; Ehrenberg, H. Chemical, Structural, and Electronic Aspects of Formation and Degradation Behavior on Different Length Scales of Ni-Rich NCM and Li-Rich HE-NCM Cathode Materials in Li-Ion Batteries. *Adv. Mater.* **2019**, *31*, No. 1900985.

(2) Park, K. J.; Jung, H. G.; Kuo, L. Y.; Kaghazchi, P.; Yoon, C. S.; Sun, Y. K. Improved Cycling Stability of Li[$Ni_{0.90}Co_{0.05}Mn_{0.05}$]$O_2$ Through Microstructure Modification by Boron Doping for Li-Ion Batteries. *Adv. Energy Mater.* **2018**, *8*, No. 1801202.

(3) Yan, P.; Zheng, J.; Liu, J.; Wang, B.; Cheng, X.; Zhang, Y.; Sun, X.; Wang, C.; Zhang, J.-G. Tailoring Grain Boundary Structures and Chemistry of Ni-rich Layered Cathodes for Enhanced Cycle Stability of Lithium-ion Batteries. *Nat. Energy* **2018**, *3*, 600−605.

(4) Zhao, W.; Zheng, J.; Zou, L.; Jia, H.; Liu, B.; Wang, H.; Engelhard, M. H.; Wang, C.; Xu, W.; Yang, Y.; Zhang, J. G. High Voltage Operation of Ni-Rich NMC Cathodes Enabled by Stable Electrode/Electrolyte Interphases. *Adv. Energy Mater.* **2018**, *8*, No. 1800297.

(5) Radin, M. D.; Hy, S.; Sina, M.; Fang, C.; Liu, H.; Vinckeviciute, J.; Zhang, M.; Whittingham, M. S.; Meng, Y. S.; Van der Ven, A. Narrowing the Gap between Theoretical and Practical Capacities in Li-Ion Layered Oxide Cathode Materials. *Adv. Energy Mater.* **2017**, *7*, No. 1602888.

(6) Ran, Q.; Zhao, H.; Hu, Y.; Shen, Q.; Liu, W.; Liu, J.; Shu, X.; Zhang, M.; Liu, S.; Tan, M.; Li, H.; Liu, X. Enhanced Electrochemical Performance of Dual-conductive Layers Coated Ni-Rich Li-$Ni_{0.6}Co_{0.2}Mn_{0.2}O_2$ Cathode for Li-ion Batteries at High Cut-off Voltage. *Electrochim. Acta* **2018**, *289*, 82−93.

(7) Cho, W.; Lim, Y. J.; Lee, S. M.; Kim, J. H.; Song, J. H.; Yu, J. S.; Kim, Y. J.; Park, M. S. Facile Mn Surface Doping of Ni-Rich Layered Cathode Materials for Lithium Ion Batteries. *ACS Appl. Mater. Interfaces* **2018**, *10*, 38915−38921.

(8) Liang, J. Y.; Zeng, X. X.; Zhang, X. D.; Wang, P. F.; Ma, J. Y.; Yin, Y. X.; Wu, X. W.; Guo, Y. G.; Wan, L. J. Mitigating Interfacial Potential Drop of Cathode-Solid Electrolyte via Ionic Conductor Layer To Enhance Interface Dynamics for Solid Batteries. *J. Am. Chem. Soc.* **2018**, *140*, 6767−6770.

(9) Pan, H.; Zhang, S.; Chen, J.; Gao, M.; Liu, Y.; Zhu, T.; Jiang, Y. Li- and Mn-rich Layered Oxide Cathode Materials for Lithium-ion Batteries: a Review from Fundamentals to Research Progress and Applications. *Mol. Syst. Des. Eng.* **2018**, *3*, 748−803.

(10) Li, W.; Asl, H. Y.; Xie, Q.; Manthiram, A. Collapse of $LiNi_{1-x-y}Co_xMn_yO_2$ Lattice at Deep Charge Irrespective of Nickel Content in Lithium-Ion Batteries. *J. Am. Chem. Soc.* **2019**, *141*, 5097−5101.

(11) Tang, M.; Yang, J.; Chen, N.; Zhu, S.; Wang, X.; Wang, T.; Zhang, C.; Xia, Y. Overall Structural Modification of a Layered Ni-rich Cathode for Enhanced Cycling Stability and Rate Capability at High Voltage. *J. Mater. Chem. A* **2019**, *7*, 6080−6089.

(12) Li, X.; Liu, J.; Banis, M. N.; Lushington, A.; Li, R.; Cai, M.; Sun, X. Atomic Layer Deposition of Solid-state Electrolyte Coated Cathode Materials with Superior High-voltage Cycling Behavior for Lithium ion Battery Application. *Energy Environ. Sci.* **2014**, *7*, 768−778.

(13) Lee, M. J.; Noh, M.; Park, M. H.; Jo, M.; Kim, H.; Nam, H.; Cho, J. The Role of Nanoscale-Range Vanadium Treatment in $LiNi_{0.8}Co_{0.15}Al_{0.05}O_2$ Cathode Materials for Li-ion Batteries at Elevated Temperatures. *J. Mater. Chem. A* **2015**, *3*, 13453−13460.

(14) Fan, Q.; Yang, S.; Liu, J.; Liu, H.; Lin, K.; Liu, R.; Hong, C.; Liu, L.; Chen, Y.; An, K.; Liu, P.; Shi, Z.; Yang, Y. Mixed-conducting Interlayer Boosting the Electrochemical Performance of Ni-rich Layered Oxide Cathode Materials for Lithium ion Batteries. *J. Power Sources* **2019**, *421*, 91−99.

(15) Jo, C. H.; Cho, D. H.; Noh, H. J.; Yashiro, H.; Sun, Y. K.; Myung, S. T. An Effective Method to Reduce Residual Lithium Compounds on Ni-rich $Li[Ni_{0.6}Co_{0.2}Mn_{0.2}]O_2$ Active Material Using a Phosphoric Acid Derived Li_3PO_4 Nanolayer. *Nano Res.* **2015**, *8*, 1464−1479.

(16) Cho, Y.; Oh, P.; Cho, J. A New Type of Protective Surface Layer for High-capacity Ni-Based Cathode Materials: Nanoscaled Surface Pillaring Layer. *Nano Lett.* **2013**, *13*, 1145−1152.

(17) Woo, S. G.; Kim, J. H.; Kim, H. R.; Cho, W.; Yu, J. S. Failure Mechanism Analysis of $LiNi_{0.88}Co_{0.09}Mn_{0.03}O_2$ Cathodes in Li-ion Full Cells. *J. Electroanal. Chem.* **2017**, *799*, 315−320.

(18) Salitra, G.; Markevich, E.; Afri, M.; Talyosef, Y.; Hartmann, P.; Kulisch, J.; Sun, Y. K.; Aurbach, D. High-Performance Cells Containing Lithium Metal Anodes, $LiNi_{0.6}Co_{0.2}Mn_{0.2}O_2$ (NCM 622) Cathodes, and Fluoroethylene Carbonate-Based Electrolyte Solution with Practical Loading. *ACS Appl. Mater. Interfaces* **2018**, *10*, 19773−19782.

(19) Xiong, X.; Ding, D.; Bu, Y.; Wang, Z.; Huang, B.; Guo, H.; Li, X. Enhanced Electrochemical Properties of a $LiNiO_2$-based Cathode Material by Removing Lithium Residues with $(NH_4)_2HPO_4$. *J. Mater. Chem. A* **2014**, *2*, 11691−11696.

(20) Zhou, P.; Zhang, Z.; Meng, H.; Lu, Y.; Cao, J.; Cheng, F.; Tao, Z.; Chen, J. SiO2-coated $LiNi_{0.915}Co_{0.075}Al_{0.01}O_2$ Cathode Material for Rechargeable Li-ion Batteries. *Nanoscale* **2016**, *8*, 19263−19269.

(21) Liu, Y.; Qian, K.; He, J.; Chu, X.; He, Y.-B.; Wu, M.; Li, B.; Kang, F. In-situ Polymerized Lithium Polyacrylate (PAALi) as Dual-functional Lithium Source for High-performance Layered Oxide Cathodes. *Electrochim. Acta* **2017**, *249*, 43−51.

(22) Lee, Y.; Lee, J.; Lee, K. Y.; Mun, J.; Lee, J. K.; Choi, W. Facile Formation of a Li_3PO_4 Coating Layer During the Synthesis of a Lithium-rich Layered Oxide for High-capacity Lithium-ion Batteries. *J. Power Sources* **2016**, *315*, 284−293.

(23) Lin, Q.; Guan, W.; Meng, J.; Huang, W.; Wei, X.; Zeng, Y.; Li, J.; Zhang, Z. A New Insight into Continuous Performance Decay Mechanism of Ni-rich Layered Oxide Cathode for High Energy Lithium ion Batteries. *Nano Energy* **2018**, *54*, 313−321.

(24) Chae, B.-J.; Park, J. H.; Song, H. J.; Jang, S. H.; Jung, K.; Park, Y. D.; Yim, T. Thiophene-initiated Polymeric Artificial Cathode-electrolyte Interface for Ni-rich Cathode Material. *Electrochim. Acta* **2018**, *290*, 465−473.

(25) Becker, D.; Borner, M.; Nolle, R.; Diehl, M.; Klein, S.; Rodehorst, U.; Schmuch, R.; Winter, M.; Placke, T. Surface Modification of Ni-Rich $LiNi_{0.8}Co_{0.1}Mn_{0.1}O_2$ Cathode Material by Tungsten Oxide Coating for Improved Electrochemical Performance in Lithium-Ion Batteries. *ACS Appl. Mater. Interfaces* **2019**, *11*, 18404−18414.

(26) Chong, J.; Xun, S.; Zhang, J.; Song, X.; Xie, H.; Battaglia, V.; Wang, R. Li_3PO_4-coated $LiNi_{0.5}Mn_{1.5}O_4$: a Stable High-voltage Cathode Material for Lithium-ion Batteries. *Chem. - Eur. J.* **2014**, *20*, 7479−7485.

(27) Wang, M.; Zhang, R.; Gong, Y.; Su, Y.; Xiang, D.; Chen, L.; Chen, Y.; Luo, M.; Chu, M. Improved Electrochemical Performance of the $LiNi_{0.8}Co_{0.1}Mn_{0.1}O_2$ Material with Lithium-ion Conductor Coating for Lithium-ion Batteries. *Solid State Ionics* **2017**, *312*, 53−60.

(28) Wu, F.; Zhang, X.; Zhao, T.; Li, L.; Xie, M.; Chen, R. Surface Modification of a Cobalt-free Layered $Li[Li_{0.2}Fe_{0.1}Ni_{0.15}Mn_{0.55}]O_2$ Oxide with the $FePO_4/Li_3PO_4$ Composite as the Cathode for Lithium-ion Batteries. *J. Mater. Chem. A* **2015**, *3*, 9528−9537.

(29) An, K.; Skorpenske, H. D.; Stoica, A. D.; Ma, D.; Wang, X. L.; Cakmak, E. First In Situ Lattice Strains Measurements Under Load at VULCAN. *Metall. Mater. Trans. A* **2011**, *42*, 95−99.

(30) An, K.; Wang, X. L.; Stoica, A. D. *Vulcan Data Reduction and Interactive Visualization Software*, 2012.

(31) Larson, A. C.; Dreele, R. B. V. *General Structure Analysis System (GSAS)*, Los Alamos National Laboratory Report (LAUR), 2004; pp 86−748.

(32) Toby, B. H. EXPGUI, A Graphical User Interface for GSAS. *J. Appl. Crystallogr.* **2001**, *34*, 210−213.

(33) Liu, H.; Liu, H.; Seymour, I. D.; Chernova, N.; Wiaderek, K. M.; Trease, N. M.; Hy, S.; Chen, Y.; An, K.; Zhang, M.; Borkiewicz, O. J.; Lapidus, S. H.; Qiu, B.; Xia, Y.; Liu, Z.; Chupas, P. J.; Chapman, K. W.; Whittingham, M. S.; Grey, C. P.; Meng, Y. S. Identifying the Chemical and Structural Irreversibility in $LiNi_{0.8}Co_{0.15}Al_{0.05}O_2$ − a Model Compound for Classical Layered Intercalation. *J. Mater. Chem. A* **2018**, *6*, 4189−4198.

(34) Liu, H.; Liu, H.; Lapidus, S. H.; Meng, Y. S.; Chupas, P. J.; Chapman, K. W. Sensitivity and Limitations of Structures from X-ray and Neutron-Based Diffraction Analyses of Transition Metal Oxide Lithium-Battery Electrodes. *J. Electrochem. Soc.* **2017**, *164*, A1802−A1811.

(35) Li, X.; Zhang, K.; Wang, S.; Wang, M.; Jiang, F.; Liu, Y.; Huang, Y.; Zheng, J. Optimal Synthetic Conditions for a Novel and High Performance Ni-rich Cathode Material of $LiNi_{0.68}Co_{0.10}Mn_{0.22}O_2$. *Sustainable Energy Fuels* **2018**, *2*, 1772−1780.

(36) Zhao, J.; Zhang, W.; Huq, A.; Misture, S. T.; Zhang, B.; Guo, S.; Wu, L.; Zhu, Y.; Chen, Z.; Amine, K.; Pan, F.; Bai, J.; Wang, F. In Situ Probing and Synthetic Control of Cationic Ordering in Ni-Rich Layered Oxide Cathodes. *Adv. Energy Mater.* **2017**, *7*, No. 1601266.

(37) Liu, H.; Fell, C. R.; An, K.; Cai, L.; Meng, Y. S. In-situ Neutron Diffraction Study of the $xLi_2MnO_{3·(1−x)}LiMO2$ (x = 0, 0.5; M = Ni, Mn, Co) Layered Oxide Compounds during Electrochemical Cycling. *J. Power Sources* **2013**, *240*, 772−778.

(38) Tian, L.; Liang, K.; Wen, X.; Shi, K.; Zheng, J. Enhanced Cycling Stability and Rate Capability of $LiNi_{0.80}Co_{0.15}Al_{0.05}O_2$ Cathode Material by a Facile Coating Method. *J. Electroanal. Chem.* **2018**, *812*, 22−27.

(39) Liang, C.; Kong, F.; Longo, R. C.; Zhang, C.; Nie, Y.; Zheng, Y.; Cho, K. Site-dependent Multicomponent Doping Strategy for Ni-rich $LiNi_{1−2y}Co_yMn_yO_2$ (y = 1/12) Cathode Materials for Li-ion Batteries. *J. Mater. Chem. A* **2017**, *5*, 25303−25313.

(40) Gent, W. E.; Lim, K.; Liang, Y.; Li, Q.; Barnes, T.; Ahn, S. J.; Stone, K. H.; McIntire, M.; Hong, J.; Song, J. H.; Li, Y.; Mehta, A.; Ermon, S.; Tyliszczak, T.; Kilcoyne, D.; Vine, D.; Park, J. H.; Doo, S. K.; Toney, M. F.; Yang, W.; Prendergast, D.; Chueh, W. C. Coupling between Oxygen Redox and Cation Migration Explains Unusual Electrochemistry in Lithium-rich Layered Oxides. *Nat. Commun.* **2017**, *8*, No. 2091.

(41) Wang, X.; Hao, H.; Liu, J.; Huang, T.; Yu, A. A Novel Method for Preparation of Macroposous Lithium Nickel Manganese Oxygen as Cathode Material for Lithium ion Batteries. *Electrochim. Acta* **2011**, *56*, 4065−4069.

(42) Zhao, X.; Liang, G.; Lin, D. Synthesis and Characterization of Al-substituted $LiNi_{0.5}Co_{0.2}Mn_{0.3}O_2$ Cathode Materials by a Modified Co-precipitation Method. *RSC Adv.* **2017**, *7*, 37588−37595.

(43) Kim, T.; Ono, L. K.; Fleck, N.; Raga, S. R.; Qi, Y. Transition Metal Speciation as a Degradation Mechanism with the Formation of a Solid-electrolyte Interphase (SEI) in Ni-rich Transition Metal Oxide Cathodes. *J. Mater. Chem. A* **2018**, *6*, 14449−14463.

(44) Park, K.; Park, J. H.; Hong, S. G.; Choi, B.; Seo, S. W.; Park, J. H.; Min, K. Enhancement in The Electrochemical Performance of Zirconium/phosphate Bi-functional Coatings on Li-$Ni_{0.8}Co_{0.15}Mn_{0.05}O_2$ by the Removal of Li Residuals. *Phys. Chem. Chem. Phys.* **2016**, *18*, 29076−29085.

(45) Razmjoo Khollari, M. A.; Paknahad, P.; Ghorbanzadeh, M. Improvement of the Electrochemical Performance of a Nickel Rich $LiNi_{0.5}Co_{0.2}Mn_{0.3}O_2$ Cathode Material by Reduced Graphene Oxide/ SiO_2 Nanoparticle Double-layer Coating. *New J. Chem.* **2019**, *43*, 2766−2775.